# DEM Analysis of the Effect of Lamination Properties on the Stability of an Underground Coal Mine Entry with Laminated Shale Roof

**Article** *in* Mining Metallurgy & Exploration · January 2022

CITATIONS
0

READS
93

**3 authors:**

Qingwen Shi
West Virginia University
**7** PUBLICATIONS **9** CITATIONS
SEE PROFILE

Brijes Mishra
University of Utah
**49** PUBLICATIONS **275** CITATIONS
SEE PROFILE

Zhao Yun
West Virginia University
**2** PUBLICATIONS **1** CITATION
SEE PROFILE

Mining, Metallurgy & Exploration
https://doi.org/10.1007/s42461-022-00541-z

# DEM Analysis of the Effect of Lamination Properties on the Stability of an Underground Coal Mine Entry with Laminated Shale Roof

**Qingwen Shi**[1] · **Brijes Mishra**[1] · **Yun Zhao**[1]

Received: 11 August 2021 / Accepted: 4 January 2022


**Abstract**
The effect of discontinuities on the fracturing and mechanical behavior of shale has been extensively investigated on a laboratory scale in previous works. It is well agreed that the lamination properties, including discontinuity and lamina properties, affect the behavior of shale. However, it is still unclear how the lamination properties are affecting the stability of the shale roof in an underground coal mine entry. This paper investigated the effect of lamination properties using discrete element method on a mine-scale entry model as an extension to the previous work conducted on laboratory scale models (Q. Shi and B. Mishra, Discrete Element Modeling of Delamination in Laboratory Scale Laminated Rock, Mining, Metallurgy & Exploration, vol. 37, no. 5, pp. 1–14, Sep. 2020). The microparameters for both the laminas and discontinuities were calibrated with laboratory data. In the calibration, a numerical laminated Brazilian disc was created and tested for comparison with laboratory results. The effects of lamina thickness, discontinuity strength, and supporting pressure on the model's roof strength and the stress distribution were also investigated. Numerical results showed that the lamination properties and supporting pressure contribute significantly to the stress distribution in the roof and its stability. The horizontal stress at a fixed depth in the roof increased with the lamina thickness, discontinuity strength, and supporting pressure. The laminated roof strength was found to increase with the increase of lamina thickness but never exceeds the strength of an intact roof comprising the only matrix.

**Keywords** Lamination properties · Stability of shale roof · Discrete element method · Discontinuity strength · Supporting pressure

## 1 Introduction

Shale is a fine-grained detrital sedimentary rock that is characterized by its finely laminated structure [1]. Laminated shale is commonly found in mines located in the Appalachian Region in the USA [2]. Roof failure commonly occurs in the entries, especially three- or four-way intersections. Due to extensive research, the number of accidents due to roof failure has significantly reduced in the past decades. However, the failure occurrence is erratic. The shale roof constitutes multiple parallelly distributed discontinuities and fails with a particular failure mode named kink or cutter roof failure as shown in Fig. 1. This type of failure causes significant damage to property and lives in the underground mining industry [3]–[4]. Previous studies observed that the lamination properties, including lamina thickness, discontinuity strength, and discontinuity orientation, have a predominant effect on shale failure [5]–[6]. Therefore, the effect of lamination properties on the stability of the shale roof should be carefully investigated.

Among these influential factors, the effects of the discontinuity orientation on the anisotropy and strength of shale have been investigated through Brazilian tests, uniaxial compressive test, and other laboratory tests, all pointing out that the orientation of the discontinuities has a significant effect on both fracture propagation and strength of the shale sample. For example, Dou et al. [8], Yang et al. [9], and Sherizadeh and Kulatilake [10] observed the micro-level failure behavior and validated that discontinuity orientation contributes to the anisotropy of the shale. Chong et al. [11] studied the sensitivity of discontinuity properties' effect on the fracturing behavior of shale, with different plane orientations. Their results show that discontinuity strength affects the shale strength while the shear-to-tensile strength ratio controls the failure pattern. Feng et al. [12] experimentally

✉ Qingwen Shi
wvuqingwenshi@gmail.com

[1] Department of Mining Engineering, West Virginia University, Morgantown, WV 26505, USA

Published online: 11 January 2022

**Fig. 1** Cutter roof failure of shale roof [2, 7]

studied the mechanical behavior of a shale Brazilian disc under different discontinuity orientations and various loading rates. Results show that both the split modulus and the absorbed energy had the minimum values when the discontinuity's inclination angle equals 45°. They also concluded that the Brazilian split strength, split modulus, and absorbed energy of shale gradually increase with the increase in loading rate. Morgan and Einstein[13] demonstrated the initiation of both tensile and shear cracks along the discontinuities in Opalinus shale samples subjected to uniaxial compression test. Bai and Tu[14] numerically pointed out that parallel discontinuities and vertical joints governed the progressive failure of the laminated roof.

Significant progress has also been made on the effect of the mechanical parameters of discontinuities on the fracturing behavior of shale. Due to the difficulty of controlling mechanical parameters of discontinuities in the lab, the present research was performed using numerical methods. Yang et al. [9] and Dou et al. [8] conducted a parametric study on Brazilian test discs and three-point bending test blocks respectively, revealing the importance of discontinuity strength on the anisotropic behavior of the shale. The same trend was also observed by He et al. [15], Heng et al. [16], and Jia et al. [17].

In addition, some studies focused on the effect of the lamina parameters in a laminated shale model. For example, Esterhuizen and Bajpayee[5] pointed out that the buckling failure mode tends to occur within a certain lamina thickness which varies from 6 to 15 cm. Jia et al. [17] found that the number of fractures decreases gradually with the increase of lamina thickness in simulated wellbores using a bonded particle material (BPM). Abousleiman et al. [6] conducted a sensitivity analysis of influential factors of the bedded coal mine roof's self-stability using UDEC. Their results showed that the self-supporting capacity is not only influenced by entry depth, fine-scale lamina, but the lamina properties such as stiffness and strength have an impact, too.

In terms of the laminated roof in coal mines, reported work emphasized the effect of horizontal stress and mine entry orientation on the roof stability [18]–[19]. The effect of the support system was also studied for years. For example, Esterhuizen and Bajpayee[5] stated that the supporting pressures would have to be impractically high to prevent horizontal stress-related damage of the laminated roof rocks by observing the ground response curve in the FLAC model. Ghabraie et al. [20] studied the mechanism of truss bolt systems, showing that these support systems can prevent shear crack propagation by repositioning the natural reinforced arch and reducing the area of loosened rock above the roof. Bai and Tu [14] numerically validated the effect of confinement provided by roof skin support with a metal mesh to restrict progressive spalling in a laminated roof.

In summary, previous research mainly focused on the effect of lamination properties on laboratory scale samples either numerically or experimentally. Similar research on the shale roof of a coal mine entry predominately aimed at the effect of support system on controlling the shale roof failure. However, the detailed effect of these lamination properties, including lamina thickness and discontinuity strength, was not investigated.

Shi and Mishra [21] studied the delamination process with a laboratory-scale discrete element method (DEM). As a follow-up, the present study established an underground entry model with a laminated roof using DEM. The effects of the lamination properties of shale on the stability of the modeled entry are investigated. The microparameters of the entry model were calibrated with laboratory data. This was then followed by a parametric analysis to investigate the effect and sensitivity of lamina thickness, discontinuity strength, and supporting pressure on the roof stability and stress distribution inside the laminated roof.

## 2 Calibration of Numerical Laminated Shale

The discrete element method particle flow code in two dimensions (PFC2D) was used in the present study. The laminated shale roof in the study was simulated by an assembly of 2D rigid particles bonded together. The laminated shale roof comprises laminas and distributed discontinuities. In this study, the laminas were modeled with a linear parallel

**Table 1** Brazilian tensile strength (BTS) of the shale samples [15]

| θ | Brazilian tensile strength, MPa | | | |
|---|---|---|---|---|
| | 0° | 30° | 60° | 90° |
| 1 | 8.129 | 4.229 | 4.718 | 2.789 |
| 2 | 6.264 | 7.098 | 3.243 | 3.505 |
| 3 | 5.567 | 6.583 | 3.623 | 3.566 |
| 4 | 7.936 | 5.265 | 3.025 | 2.944 |
| 5 | 7.458 | 4.986 | 2.857 | 2.654 |
| Mean | 7.071 | 5.632 | 0.664 | 3.091 |

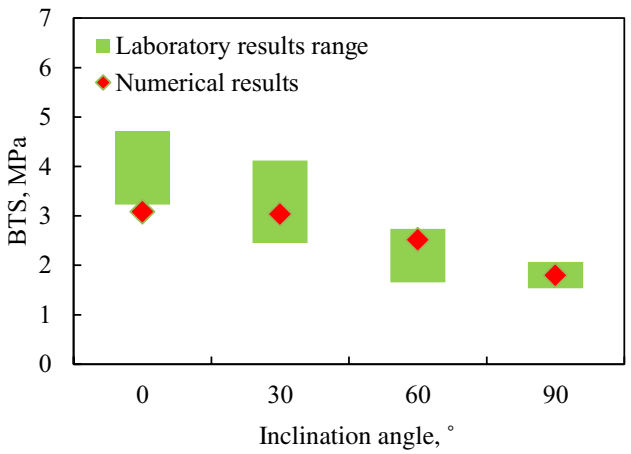


**Fig. 2** Comparison between numerical and experimental results of the laminated specimen under Brazilian test

bonded model [22, 23] and the discontinuities were modeled with a smooth-joint model [23] provided in PFC.

The Brazilian tensile strength of the shale from the literature survey [15] was used for calibrating the model microparameters. In the present study, the test results with inclination angles of 0°, 30°, 60°, and 90° were used, as shown in Table 1.

There is no efficient way to calibrate the assembly comprising both the linear parallel bond model and the smooth-joint model. Researchers must adjust the microparameters through trial and error based on observation of the failure mode and failure strength. We must note that the laboratory test results must be scaled when they are applied to large-scale rock mass during the calibration. In the present research, the strength reduction factor of 0.58 [24, 25] is used for the BPM with discontinuities. After multiple iterations of trial and error, both numerical and scaled experimental Brazilian tensile strength results of the laminated specimens are presented in Fig. 2 at different inclination angles. Generally, the numerical model results show a good match with the experimental results.

Typical fracture patterns for different inclination angles of the shale specimens are shown in Fig. 3 [15]. It is concluded that the fracture patterns vary with the inclination angle. Central-linear/curved fracture mainly propagated along the loading axis when the orientation was 0° and 90°. In the specimens with the inclination angles of 30° and 60°, the fractures mainly develop along the lamina direction or with some orthogonal fractures. However, the failure tends to occur near the loading point in a 30° inclined specimen. The calibrated fracture patterns are given in Fig. 4, wherein the blue lines represent the tensile cracks and the red lines represent the shear cracks. Compared with Fig. 3, the fracture patterns in the numerical model match well with laboratory results. This further validated the reliability of our calibrated microparameters. The numerical models utilizing these microparameters can capture the fracturing behavior of the laminated shale.

## 3 Configuration and Empirical Verification of the Entry Models

In the present section, the entry model incorporating laminated shale roof, coal seam, and the floor was created. The entry excavation was simulated by deleting the particles within the entry domain. Then, the entry model was verified by comparing the roof failure modes of the intact roof


**Fig. 3** Fracture patterns of slate specimens with different inclination angles [15]

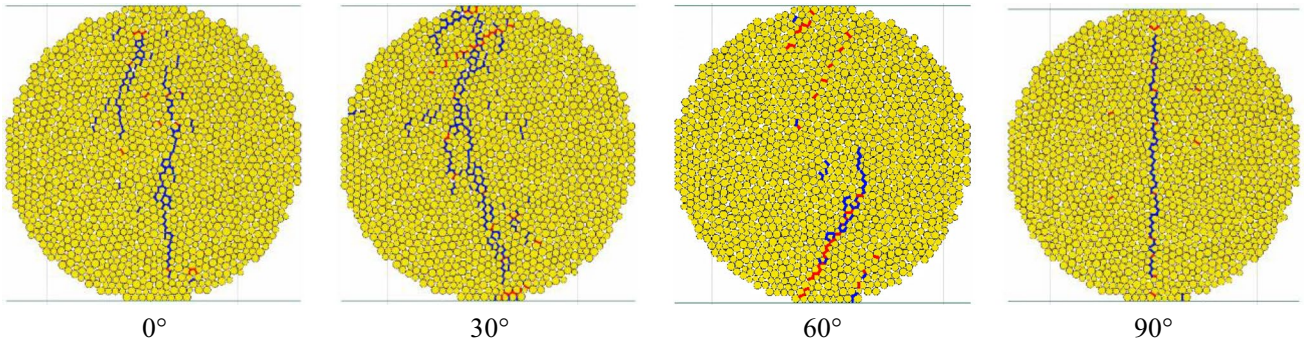


**Fig. 4** Fracture patterns of calibrated models

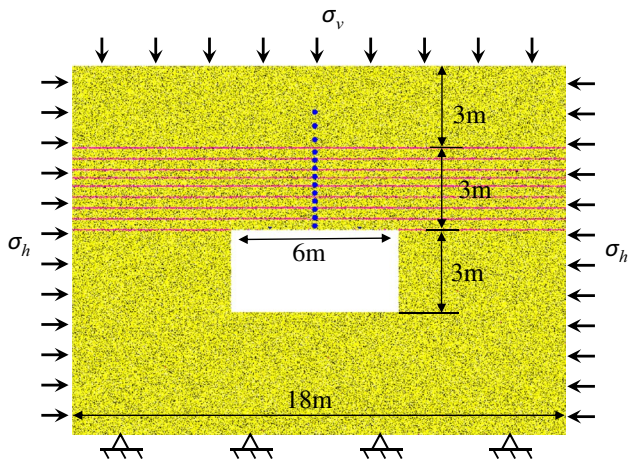


**Fig. 5** Schematic diagram and boundary conditions of the entry model ($\sigma_h$ corresponds to the horizontal stress while $\sigma_v$ corresponds to the vertical stress; blue dots represent the measure stations set in the model roof)

and laminated roof. Moreover, the model results obtained from sensitivity analysis, which were provided in detail in Section 4, were compared to an empirical evaluation of roof-support effectiveness (ARBS) in the context of the coal mine roof rating (CMRR) system.

### 3.1 Configuration of the Entry Model Incorporating Shale Roof

In PFC, a slight increase in the model size brings a significant increase in the run-time. Therefore, the dimension of the model should be carefully considered. In the present study, the dimensions of the entry model are set to 18 × 13.5 m. The model comprises a 3-m-thick laminated roof, above which is a competent roof that has no discontinuities. The schematic diagram of the entry model is shown in Fig. 5. The laminated roof incorporates laminas simulated with linear parallel bonded model and discontinuities simulated with smooth joints

**Table 2** Microparameters of laminas used in the PFC2D model

| Micro-parameter | Value |
|---|---|
| Particle density, kg/m$^3$ | 2610 |
| Particle size, mm | 10 to 15 |
| Damping ratio | 0.5 |
| Bond gap, m | $5\times10^{-4}$ |
| Young's modulus of the particle, GPa | 10 |
| Young's modulus of the parallel bond, GPa | 10 |
| Ratio of normal to shear stiffness of the particle | 1.0 |
| Ratio of normal to shear stiffness of the parallel bond | 1.0 |
| Particle friction coefficient | 0.7 |
| Parallel bond tensile strength, MPa | 11 |
| Parallel bond cohesion, MPa | 60 |
| Friction angle, degree | 31 |

Microparameters listed in this table are for linear parallel bonded model

Microparameters listed in this table achieved a match with scaled laboratory results

**Table 3** Microparameters of discontinuities used in the PFC2D model

| Microparameter | Value |
|---|---|
| Discontinuity distance, mm | 20 |
| Normal stiffness of smooth joint, GPa/m | 100 |
| Shear stiffness of smooth joint, GPa/m | 2000 |
| Tensile strength of smooth joint, MPa | 2 |
| Shear strength of smooth joint, MPa | 15 |
| Friction coefficient | 0.6 |
| Contact gap, m | $5\times10^{-4}$ |

Microparameters listed in this table are for smooth joint model

Microparameters listed in this table achieved a match with scaled laboratory results

model. The microparameters of laminas and discontinuities calibrated in Section 2 to replicate scaled experimental results are listed in Table 2 and Table 3

respectively. The objective of the present research is to investigate the lamination properties' effect on roof failure. Therefore, the competent roof, coal body, and floor are hypothetically set the same with lamina parameters listed in Table 2 corresponding to a linear parallel bonded model.

The bottom of the model was fixed while vertical and horizontal stresses were applied to the top and both sides of the model respectively as shown in Fig. 5. The model simulates the typical stress conditions that one might expect at a depth of 390 m, which typically represents a vertical stress $\sigma_v$ of 10.0 MPa. The model was run for different horizontal stress magnitudes to find the minimum horizontal stress value that can cause roof failure. This value was defined as the critical failure stress of the model in the present study. As an example, we started modeling with a horizontal stress of 10 MPa. If the roof did not fail, we proceeded to increase the horizontal stress stepwise until we found a value $\sigma_x$ under which the roof failure was observed. In this case, the value $\sigma_x$ is called critical failure stress for this model. The servo-mechanism [23] provided by PFC was used to apply preset stresses to the boundaries. Measurement spheres, denoted as blue dots, with a diameter of 0.2 m were placed above the roofline to monitor stress distributions after excavation.

Additionally, the default local damping was used in all models since it is most efficient for removing kinetic energy when implementing a static analysis. Considering the problem we are observing involves falling of fractured BPM, we kept removing the falling fragments (realized by manually deleting falling particles) during the calculation to ensure the models can reach equilibrium.

### 3.2 Comparison of the Laminated and Nonlaminated Models

Simulations comparing models with laminated roof and models with only competent roof, i.e., nonlaminated model, were conducted on an entry model without lamination as a comparison. The vertical stress remained constant at 10.0 MPa. The failure pattern and scope of the model without laminations (nonlaminated model) were captured under varying horizontal stress, as demonstrated in Fig. 6. The colored particles represent the fragments in the specimen and the same color indicates a piece of fragments that comprise a clump of bonded particles. Different colors of fragments indicate that the fragments are separated due to the development of the fractures. The model shows critical failure stress under which the model roof can stay stable with only minor spalling, as shown in Fig. 6a and b. When the critical failure stress is reached, however, the roof failure will keep developing upward as shown in Fig. 6c. The same phenomenon happens for the laminated model, as shown in Fig. 7c. The developing failure caused models in these cases did not converge. However, we argue this did not affect our results since the parameter we need for analysis, critical failure stress value, was obtained. Nevertheless, the two models differ significantly in failure mode. The roof failure develops in a dome-like shape in Fig. 6c while the cavity formed in the laminated model has near-vertical sides in Fig. 7c. This verified the field observation [5].

### 3.3 Empirical Comparison

In order to verify our entry models, empirical observations of roof-support effectiveness (ARBS) based on the coal mine roof rating (CMRR) were compared to numerical results

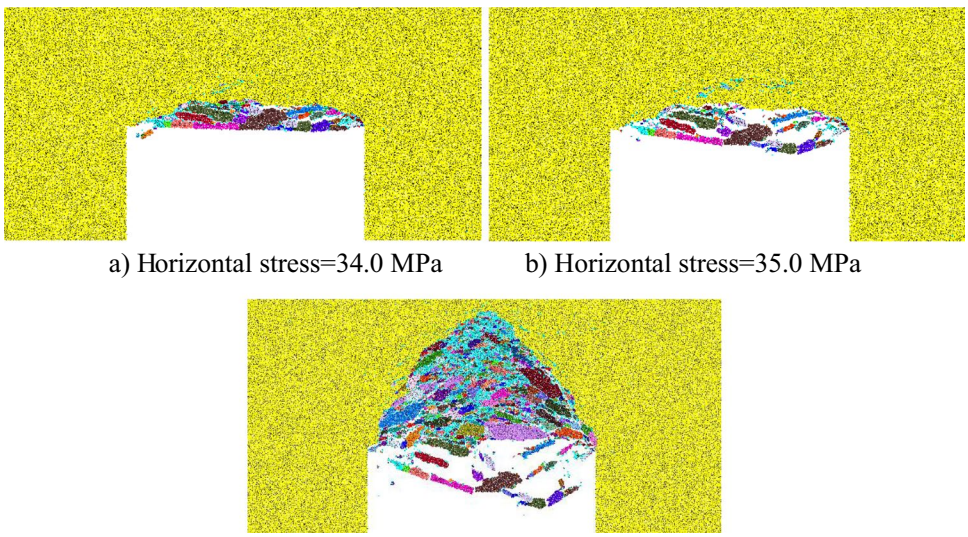

a) Horizontal stress=34.0 MPa b) Horizontal stress=35.0 MPa

c) Horizontal stress=36.0 MPa

**Fig. 6** Failure mode of a nonlaminated model with critical failure stress of 36.0 MPa (falling fragments were kept here for illustration). a. Horizontal stress = 34.0 MPa, b. Horizontal stress = 35.0 MPa, c. Horizontal stress = 36.0 MPa

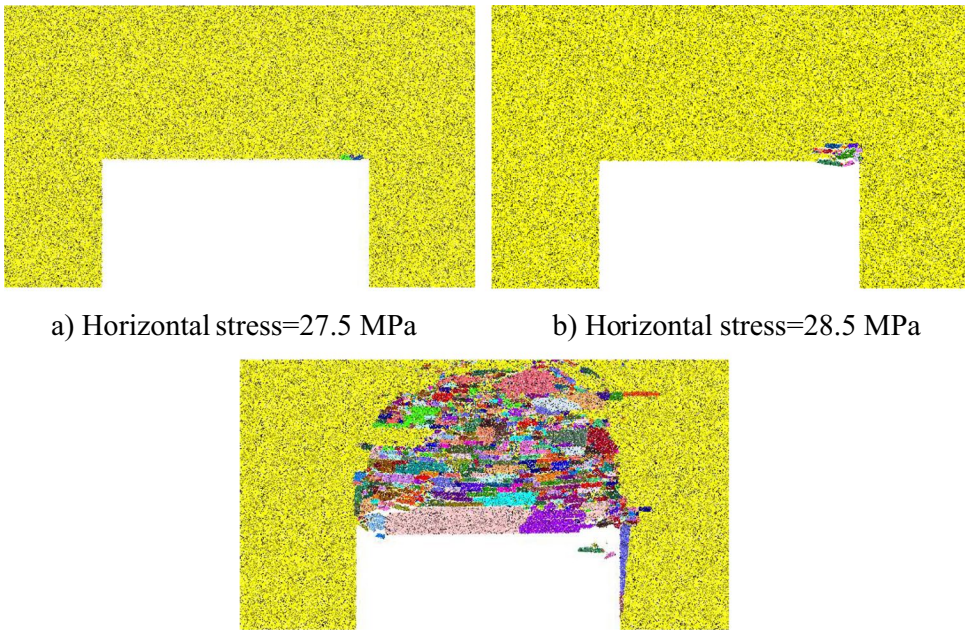


**Fig. 7** Failure mode of a laminated model with critical failure stress of 29.0 MPa (lamina thickness = 10 cm; falling fragments were kept here for illustration). a. Horizontal stress = 27.5 MPa, b. Horizontal stress = 28.5 MPa, c. Horizontal stress = 29.0 MPa

obtained in our sensitivity analysis in Section 4 that follows. CMRR is an index widely used for quantifying the overall condition of coal mine roof based on observationally or experimentally determined parameters of the roof rock. ARBS serves as an evaluation of bolt system intensity based on the pattern and capacity of bolts. A practical method to obtain a valid ARBS is given by Mark [26]. A suggested ARBS ($ARBS_G$) was also provided based on CMRR and overburden depth ($H$) of the entry as:

$$ARBS_G = (5.7\log 10H) - 0.35CMRR + 6.5 \quad (1)$$

The performance of this design methodology was validated by plotting the difference between the entry's suggested $ARBS_G$ and entry span $Is_G$ and corresponding actual ARBS and entry span Is. According to roof support results categorized as "success" or "failure," an adjustment to the suggested $ARBS_G$ was obtained according to the established linear discriminant:

$$ARBS_{Gadj} = ARBS_G - 0.3[Is_G - Is] \quad (2)$$

In the sensitivity analysis in this section, thirty-six models with different lamination setups and supporting pressure were analyzed. Critical failure stress was obtained in each case. Considering the vertical stress of 10 MPa, we assumed the horizontal stress as 25 MPa, corresponding to a normally horizontal stress coefficient of 2.5. Therefore, models with critical stress larger than 25 MPa were categorized as "Unstable" while those less than 25 MPa were categorized as "Stable."

Firstly, we evaluated the CMRR value for the laminated roof in each model following the approach provided by Molinda and Mark [27]. The unconfined compressive strength (UCS) of the model was calculated as:

$$UCS = \frac{2c \bullet \cos\varphi}{1 - \sin\varphi} \quad (3)$$

where $c$ corresponds to the cohesion of the block material, and $\varphi$ represents the friction angle of the block material. In these models, the UCS rating was therefore assigned as 30 (max). The discontinuity intensity was rated as 9 in all these models since the spacing in our models is all less than 6 cm. The discontinuity strength was evaluated with point load test strength index $Is_{(50)}$. The $Is_{(50)}$ was estimated by converting Brazilian tensile strength (BTS) using the experimental fitting results provided by [28]:

$$Is_{(50)} = 0.5654 \bullet BTS - 1.4532 \quad (4)$$

The $Is_{(50)}$ of models with various discontinuity strength ratios was determined by scaling with the discontinuity strength ratio. Therefore, a laminated roof with discontinuity strength ratios of 0.5, 0.75, 1.0, 1.25, and 1.5 modeled in Sect. 5.2 was assigned with $Is_{(50)}$ and discontinuity shear strength rating as Table 4. Moisture sensitivity rating was not counted since the present models did not consider water.

Secondly, the ARBS value was approximated based on the supporting pressure we applied in Sect. 5.3 that follows. For unsupported models, the absence of bolts introduces an ARBS value of 0. For the supported ones, the different bolt

**Table 4** Discontinuity shear strength rating estimation for models with various discontinuity strength ratios

| Discontinuity strength ratio | $Is_{(50)}$, MPa | Discontinuity shear strength rating |
|---|---|---|
| 0.5 | 0.147 | 64 |
| 0.75 | 0.221 | 64 |
| 1.0 | 0.294 | 65.154 |
| 1.25 | 0.368 | 66.693 |
| 1.5 | 0.442 | 68.231 |

design was assumed based on various supporting pressure we applied since the model only applied surface pressure that follows the skin control mechanism of the support system [26]. The assigned bolting parameters and corresponding ARBS are listed in Table 5.

Finally, we plotted the difference between the entry's suggested $ARBS_G$ and entry span $Is_G$ and corresponding actual ARBS and entry span Is as shown in Fig. 8. Figure 8 shows that predicted and actual model results in relation to ARBS discriminant for our entry models were in good agreement [26]. The lower right-hand quadrant of the graph contains 10 cases in which the formulas predict that the span was too large or supporting pressure was too low for such a roof condition. Among these cases, 9 were in fact unstable cases and only one was mistakenly predicted. The upper left-hand quadrant contains 26 cases wherein the empirical formulas predict that the span or the supporting pressure was adequate. This result indicated that empirical calculations and numerical predictions of our entry model accurately showed the relationship between CMRR, ARBS, overburden depth, and roof span. We have to note that the ARBS was developed for supported roof evaluation and may not be directly comparable to the unsupported models in the present study Table 6.

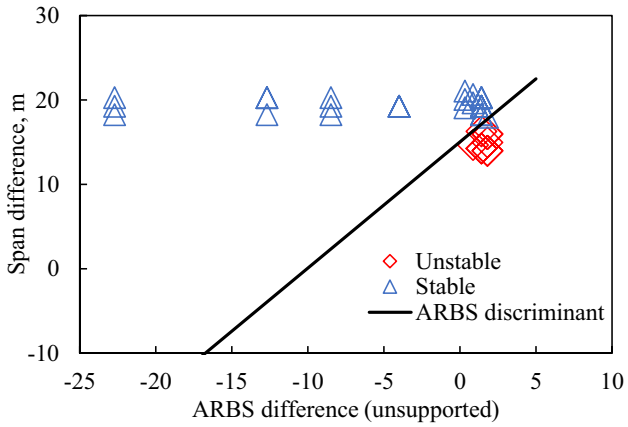


**Fig. 8** Results of entry models and their predicted stability based on empirical formulas [26]

**Table 6** Critical failure stress of the models with different plane strength

| Smooth joint strength (strength ratio) | Lamina thickness, cm | Critical failure stress, MPa |
|---|---|---|
| Tensile strength = 3.0 MPa<br>Shear strength = 22.5 MPa<br>(1.5:1) | 10 | 30.7 |
| | 20 | 33.0 |
| | 30 | 38.5 |
| Tensile strength = 2.5 MPa<br>Shear strength = 18.75 MPa<br>(1.25:1) | 10 | 27.5 |
| | 20 | 32.0 |
| | 30 | 37.5 |
| Tensile strength = 2.0 MPa<br>Shear strength = 15 MPa<br>(Set as a base) | 10 | 29.0 |
| | 20 | 31.0 |
| | 30 | 34.7 |
| Tensile strength = 1.5 MPa<br>Shear strength = 11.25 MPa<br>(0.75:1) | 10 | 22.5 |
| | 20 | 27.8 |
| | 30 | 32.0 |
| Tensile strength = 1.0 MPa<br>Shear strength = 7.5 MPa<br>(0.5:1) | 10 | 19.1 |
| | 20 | 25.4 |
| | 30 | 27.5 |

## 4 Sensitivity Analysis for Failure Behavior of Shale Roof

### 4.1 Effect of Lamina Thickness

The thickness of the laminas in a laminated roof varies from tens of centimeters to less than 1 cm [5]. It has a significant impact on the strength and failure development within the roof. The effect of lamina thickness on the laminated roof's failure behavior was studied in this section. Nine numerical simulations were conducted by changing the lamina thickness. The lamina thickness was taken as 10 cm, 15 cm,

**Table 5** ARBS determination for models with different supporting pressure

| Support pressure, MPa | Bolt length $L_b$, m | Number of bolts per row | Bolt capacity $C$, kN | Spacing between rows of bolts $S_b$, m | Entry width $W_e$, m | ARBS |
|---|---|---|---|---|---|---|
| 0.5 | 1.2 | 4 | 115.7 | 1.2 | 6.0 | 5.414 |
| 1 | 1.2 | 6 | 115.7 | 1.0 | 6.0 | 9.898 |
| 1.5 | 1.2 | 7 | 115.7 | 0.8 | 6.0 | 14.104 |
| 2 | 1.2 | 9 | 115.7 | 0.6 | 6.0 | 24.118 |

20 cm, 25 cm, 30 cm, 35 cm, 40 cm, 45 cm, and 50 cm respectively.

The variance of critical failure stress with lamina thickness is shown in Fig. 9. It is observed that the lamina thickness has a significant impact on the laminated roof's critical failure stress. Under constant vertical stress, the critical failure stress increases monotonously with an increase in the lamina thickness. Their variations are relatively steep before the lamina thickness approaches a considerable value. For example, when the lamina thickness is less than 25 cm, the critical failure stress gradient is around 0.32 MPa/cm. When the lamina thickness ranges between 25 and 40 cm, the gradient decreases to 0.12 MPa/cm. Furthermore, when the lamina thickness is larger than 40 cm, the curve becomes relatively flat. This indicates that a laminated roof's critical failure stress is highly sensitive to the lamina thickness where the lamina thickness is small, and the sensitivity gets lower when the thickness gets larger.

As a comparison, the nonlaminated model's critical failure stress, 36.0 MPa, is added to Fig. 9 as a red dash line. As can be observed, the nonlaminated model's critical failure stress becomes the upper limit of the laminated models' critical failure stress. As shown in Fig. 9, the curve keeps approaching 36.0 MPa with an increase of lamina thickness, and it never exceeds the limit. This demonstrates that the strength of the laminated roof is determined by the rock matrix that forms the laminas for given discontinuities.

In addition, the stress distribution along the vertical axis in the entry roof was observed in models with different lamina thicknesses. The vertical and horizontal stress applied to the model was maintained at 10 and 20 MPa, respectively, to observe lamina thickness's influence on stress distribution in the entry roof. The horizontal stress of 20 MPa was selected because none of the models fails under such a magnitude. Horizontal stress was extracted using the measure spheres along the entry's vertical axis in Fig. 5. Figure 10 shows the horizontal stress at various depths from the roofline under lamina thickness of 10 cm, 20 cm, and 30 cm, and nonlaminated model as a comparison. It is concluded that lamina thickness has a great impact on the stress magnitude in the laminated roof. However, the shapes of the distribution curve are similar, i.e., each curve is generally increasing within the depth of 1.65 from the roofline then becomes relatively flat with increasing depth.

A significant difference is observed among the curves under different lamina thicknesses. As shown in Fig. 10, horizontal stress in a fixed depth increases with the lamina thickness. For example, at a depth of 1.05 m, the horizontal stress in different models has a ranking of 10 cm lamina < 20 cm lamina < 30 cm lamina < nonlaminated model. The same trend happens at other depths. However, when the depth gets larger than 3 m, all the curves become relatively flat, and the difference between models gets smaller. This is because the depth of 3.0 m divides the laminated roof and competent intact roof as shown by the black dashed line in Fig. 10. In addition, the impact of excavation weakens in the far-field surrounding rock. The above results indicated that lamina thickness has a significant effect on roof strength and stress distribution.

## 4.2 Effect of Discontinuity Strength

The discontinuities in the laminations contribute predominantly to the large deformation and low strength of the laminated roof of underground entries. The effect of discontinuity strength on the laminated roof's fracturing behavior is explored in this section. Fifteen numerical simulations were conducted by simultaneously changing the smooth-joint model's tension and shear strength [29]. The smooth joint strength in Table 3 was set as a base, and the strength ratio to the base was taken as 1.5, 1.25, 1.0, 0.75, and 0.5,

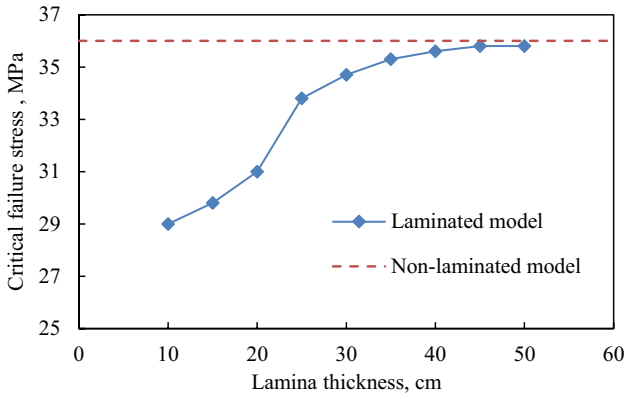


**Fig. 9** Effect of lamina thickness on critical failure stress (the red dashed line corresponds to the critical failure stress of nonlaminated model)

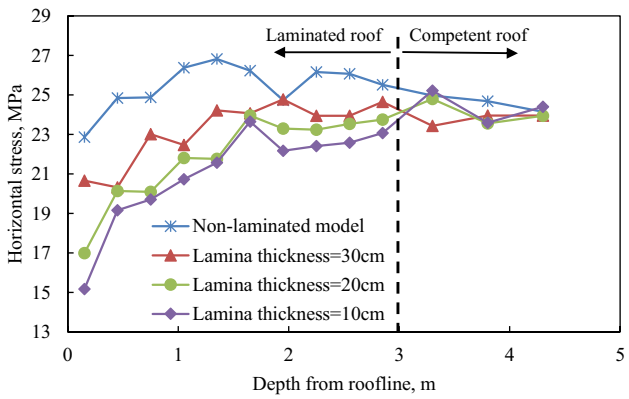


**Fig. 10** Effect of lamina thickness on stress distribution in the laminated roof (the black dashed line corresponds to the dividing line of the laminated roof and competent roof)

respectively, as shown in Table 6. All other parameters in the numerical model were kept constant.

The influence of smooth joint strength on the critical failure stress of the model is also presented in Table 4. The critical failure stress of all the models against the strength ratio with varying lamina thicknesses is shown in Fig. 11. It is observed that discontinuity strength has a significant impact on critical failure stress. Under a constant lamina thickness, the critical failure stress increases monotonously when the discontinuity strength ratio increases as shown in Fig. 11. The same trend suits the models with 20-cm- and 30-cm-thick laminas. There are some fluctuations at strength ratio = 1.25 of the 10-cm-thick model, which can be explained by the discrete element method's deviation.

In addition, a significant gap was observed among the curves under different lamina thicknesses. For example, when the strength ratio is equal to 0.5, the models' critical failure stress has a ranking of 30 cm model > 20 cm model > 10 cm model. This indicates that the effect of plane strength on critical failure stress is sensitive to the lamina thickness of the roof. The results discussed in earlier sections showed the discontinuity strength significantly affects the stability of the laminated roof of an underground entry. In general, the weaker the discontinuity strength is, the lower will be the laminated roof stability.

Also, the effect of plane strength on the stress distribution in the roof is investigated. Numerical simulations were conducted under different lamina thicknesses of 10 cm. The vertical and horizontal stress was maintained at 10 MPa and 20 MPa, respectively, for all the numerical models. All other parameters in the numerical models were kept unchanged. The variations of horizontal stress with plane strength ratio under different lamina thicknesses are shown in Fig. 12. Simulation of the stress distribution of strength ratio of 0.5 was not included in this paper as the 20-MPa horizontal stress exceeded the critical failure stress. A failed model would not reveal the stress condition induced by a laminated roof since the failure disturbed the stress distribution.

As shown in Fig. 12, the curves' shape is similar to each other. It is observed that the curve with a higher strength ratio is generally above the one with a lower strength ratio. There is a noticeable difference in the horizontal stress at a fixed depth under different strength ratios. For example, for a fixed depth of 1.35 m, the horizontal stress can be ranked as strength ratio of 0.75 < strength ratio of 1.0≈strength ratio of 1.25 < strength ratio of 1.5, indicating that the strength ratio has a significant effect on the stress distribution in the laminated roof.

### 4.3 Effect of Supporting Pressure

We investigated the influence of support systems on the initiation and development of failure of the laminated roof. The critical failure stress was used to evaluate the effect of a roof support system to control laminated roof failure. The entry models with a 3.0-m-thick shale roof containing 10-cm laminations, 20-cm laminations, and 30-cm laminations, described above, were used to compare their critical failure stress under different supporting pressures. The premining vertical stress was set at 10 MPa and the horizontal stress kept increasing stepwise until the critical failure stress is reached.

A pressure-application algorithm was adopted to simulate the support system in entries. The algorithm was initially used to apply water pressure in the drilling hole [30]. It is activated in two steps. In the first step, the algorithm identifies the particles within a certain gap on the free surface of the entry and they are connected as a chain. In the second step, the algorithm applies a specific force, which represents supporting pressure on the entry in the research, on the chained particles from outside, as depicted in Fig. 13. In Fig. 13, the orange lines are the identified chain. The red

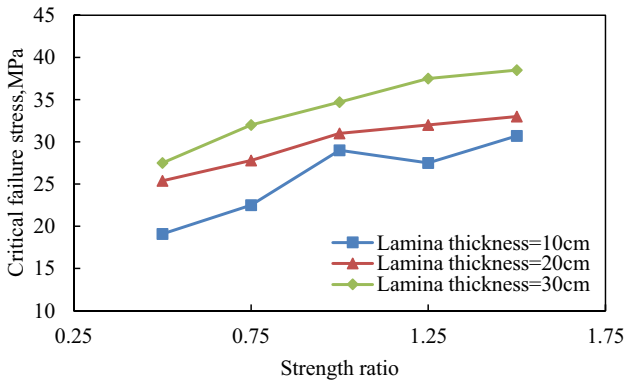


**Fig. 11** Effect of plane strength on critical failure strength of the models

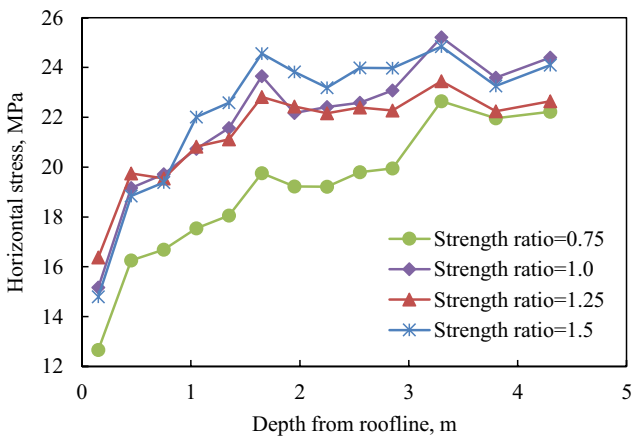


**Fig. 12** Effect of discontinuity strength ratio on stress distribution

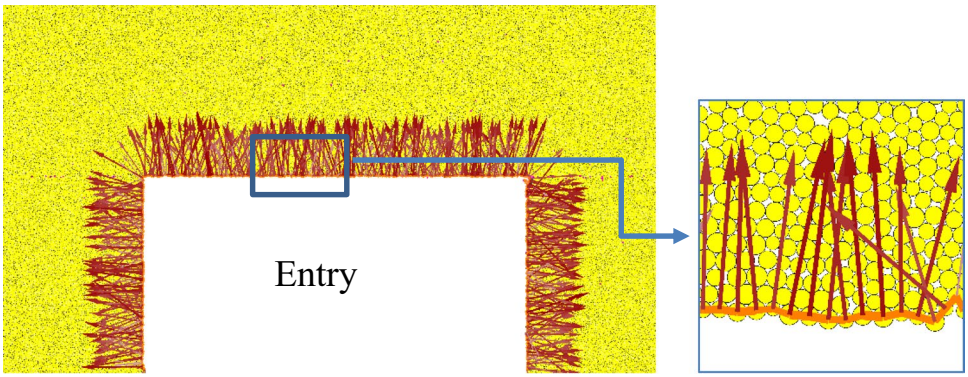


**Fig. 13** The algorithm for applying the supporting pressure

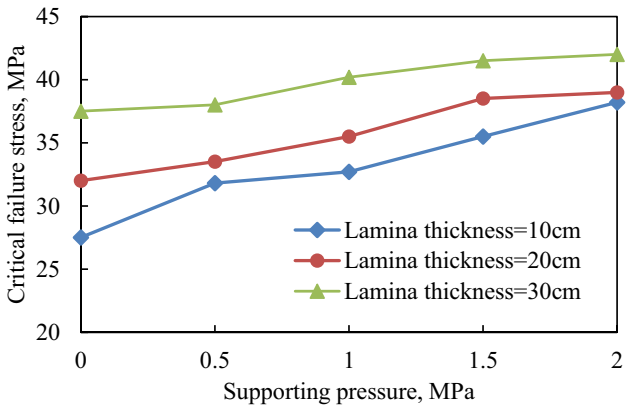


**Fig. 14** Effect of supporting pressure on critical failure stress

arrows are the force applied perpendicular to the chain. Then the complete model was calculated under a stepwise increase in the horizontal stress up to the critical failure stress.

In this study, five different assumed supporting pressures, 0 to 2 MPa with an interval of 0.5 MPa, were analyzed in the numerical models. Typically, a support design in a $0.7 \times 0.7$ m pattern with a pre-tension load of 100 kN achieves a supporting pressure of 0.2 MPa. Therefore, we have to note that the assumed supporting pressures are only for parametric study in this section since confining stress of 2 MPa is impractically high in the field.

The variations of critical failure stress of the models with supporting pressure under different lamina thicknesses are shown in Fig. 14. The critical failure stress increased monotonously with the increase in the support pressure. For a fixed support pressure, as lamina thickness increases from 10 to 30 cm, the critical failure stress of the models increased significantly. This indicated the effect of the supporting pressure to be sensitive to the lamina thickness. In addition, the gap between the curves of different lamina thicknesses decreased slightly when the support pressure is large in magnitude. For example, when the supporting pressure is 0.5 MPa, the gap between the 10 and the 30 cm curve is 5.0 MPa. When the support pressure increases to 2.0 MPa, the gap drops to 1.8 MPa. This indicates that lamina thickness has a smaller effect on roof stability for larger supporting stress.

## 5 Discussion

When comparing the failure modes of the entry model with and without laminations, a typical difference was found. The laminated roof tended to fail along a nearly vertical line at both top corners of the entry while the intact roof failed in a dome shape, which is good consistency with empirical and previous numerical observations. Empirically, Esterhuizen [5] stated that the laminated roof fall-caused cavities can have near-vertical sides, as opposed to dome-like failure cavities formed in rocks that are not bedded, which is exactly the scenario observed in our entry models. Numerically, our model results with the intact roof were consistent with that obtained with a Trigon bonded block model (BBM) [31] shown in Fig. 15a, verifying the capacity of our inputs of block material. Moreover, the laminated roof failure observed by Voronoi BBM [32] presented similar failure modes observed in our models shown in Fig. 7c, verifying the combination of block material and discontinuities' parameters.

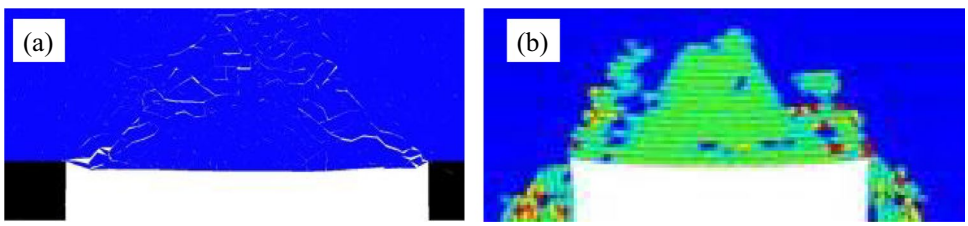


**Fig. 15** Roof failure model results using **a** intact roof simulated with Trigon BBM [31] and **b** laminated roof simulated with Voronoi BBM [32]

Since the supporting conditions in our models were different from the actual entry, a direct comparison between empirical and numerical results is not possible. However, with some appropriate assumptions discussed in Sectio 3.3, ARBS values and CMRR values of our models were obtained and used for verification. In fact, similar assumptions were made by Abousleiman [6] in their DEM models incorporating laminated roof. In their models, cutter caving and delamination of the laminated roof were categorized as unstable and a good agreement with the empirically derived ARBS discriminant was obtained. Here, we defined critical failure stress for stability evaluation. The evaluation results were consistent with the empirical observations. Our models were thus verified to have a capacity of replicating actual laminated roof.

Roof stability was found to be sensitive to the lamina thickness. When the lamina thickness is less than 25 cm, the increasing rate of the critical failure stress of the laminated roof kept increasing (Fig. 9), which is similar to the quadratic relationship between the strength of a beam and beam thickness illustrated by Euler buckling equations [5]:

$$\sigma = \frac{\pi^2 E t^2}{3L^2}$$

where $E$ is the elastic modulus and $t$ and $L$ represent the beam thickness and beam length respectively. This consistency signified a buckling failure mechanism of the laminated roof when the laminas are thin. However, when the lamina thickness gets larger, the increasing rate of critical stress decreased until 0 (Fig. 9). The possible explanation is that the laminated roof fails in compression when lamina thickness increases. This scenario is quite similar to the compression curve shown in Fig. 16 [5]. Generally, both the failure patterns and sensitivity analysis results were comparable to previous research.

## 6 Conclusions

Entry models with a laminated roof were created based on data from laboratory tests. Based on the models, failure patterns were compared between the laminated roof and the nonlaminated roof. Results showed that the laminated roof failed in a dome shape while the nonlaminated roof failed with nearly vertical sides validating the model.

The effect of lamina thickness on roof stability was investigated by evaluating models' critical failure stress. Results showed that lamina thickness significantly affects roof stability. The effect is sensitive to the lamina thickness. In addition, the laminated roof stability increases with the discontinuity strength and the maximum possible strength

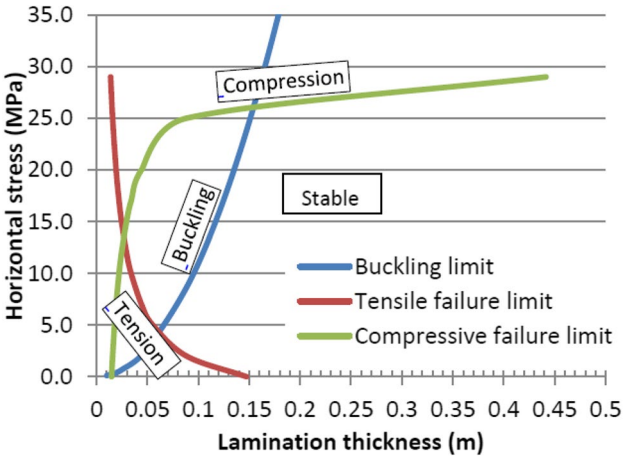


**Fig. 16** Potential failure modes of an elastic beam subject to external horizontal stress based on classic beam analysis [5]

of the laminated roof is determined by the matrix that comprised the laminas. The laminated roof's stress distribution showed that the horizontal stress magnitude at a fixed depth increases with the lamina thickness.

The effect of discontinuity strength on roof stability was investigated by changing smooth joint shear strength and tensile strength simultaneously. The roof strength increased as discontinuity strength increased. Discontinuity strength also affects the stress distribution in the roof. A high discontinuity strength can bring higher stress at a fixed depth. The effect of support pressure on the failure behavior of the shale roof was investigated using a pressure algorithm. Various supporting pressure was applied to models with different lamina thicknesses. Results show that the supporting pressure increased the stability of the laminated shale model. The increase in the supporting pressure increases the strength of the laminated roof. The effect is also sensitive to lamina thickness.

**Funding** This work was supported by National Institute for Occupational Safety and Health (NIOSH) (No. 200–2016-92214).

**Availability of Data and Material** Not applicable.

**Code Availability** Not applicable.

## Declarations

**Conflict of Interest** The authors declare no competing interests.

## References

1. O'Brien NR (1996) Shale lamination and sedimentary processes. Geol Soc Spec Publ 116(1):23–36. https://doi.org/10.1144/GSL.SP.1996.116.01.04

2. Murphy MM (2016) Shale failure mechanics and intervention measures in underground coal mines: results from 50 years of ground control safety research. Rock Mech Rock Eng 49(2):661–671. https://doi.org/10.1007/s00603-015-0861-4
3. Kuznetsov SV, Trofimov VA (2012) Formation of tension and delamination areas in a long excavation's roof. J Min Sci 48(5):789–797. https://doi.org/10.1134/s1062739148050036
4. Shi Q, Pan J, Wang S, Liu S, Mishra B, Seitz S (2021) Field monitoring of delayed coal burst in an advancing entry of a deep coal mine, *Mining*. Metall Explor 2021:1–15. https://doi.org/10.1007/S42461-021-00508-6
5. Esterhuizen GS, Bajpayee TS (2012) Horizontal stress related failure in bedded mine roofs - insight from field observations and numerical models, in *46th US Rock Mechanics*. Geomechanics Symposium 2012 1:68–77
6. Abousleiman R, Walton G, Sinha S (2020) Understanding roof deformation mechanics and parametric sensitivities of coal mine entries using the discrete element method. Int J Min Sci Technol 30(1):123–129. https://doi.org/10.1016/j.ijmst.2019.12.006
7. Molinda G, Mark C (2010) Ground failures in coal mines with weak roof. Electron J Geotech Eng 15F:1–42
8. Dou F, Wang JG, Zhang X, Wang H (2019) Effect of joint parameters on fracturing behavior of shale in notched three-point-bending test based on discrete element model. Eng Fract Mech 205:40–56. https://doi.org/10.1016/j.engfracmech.2018.11.017
9. Yang S-Q, Yin P-F, Huang Y-H (2019) Experiment and discrete element modelling on strength, deformation and failure behaviour of shale under brazilian compression, 52: 4339–4359, 2019, https://doi.org/10.1007/s00603-019-01847-z
10. Sherizadeh T, Kulatilake PHSW (2016) Assessment of roof stability in a room and pillar coal mine in the U.S. using three-dimensional distinct element method. Tunn Undergr Sp Technol. 59:24–37. https://doi.org/10.1016/j.tust.2016.06.005
11. Chong Z et al (2017) Numerical investigation of bedding plane parameters of transversely isotropic shale. Rock Mech Rock Eng 50(5):1183–1204. https://doi.org/10.1007/s00603-016-1159-x
12. Feng G, Kang Y, Wang X, Hu Y, Li X (2020) Investigation on the failure characteristics and fracture classification of shale under Brazilian test conditions. Rock Mech Rock Eng 53(7):3325–3340. https://doi.org/10.1007/s00603-020-02110-6
13. Morgan SP, Einstein HH (2014) The effect of bedding plane orientation on crack propagation and coalescence in shale, 48th US Rock Mech. Geomech Symp 3:1580–1589
14. Bai Q, Tu S (2020) Numerical observations of the failure of a laminated and jointed roof and the effective of different support schemes: a case study. Environ Earth Sci, 79(10), https://doi.org/10.1007/s12665-020-08935-2
15. He J, Afolagboye LO (2018) Influence of layer orientation and interlayer bonding force on the mechanical behavior of shale under Brazilian test conditions. Acta Mech Sin 34(2):349–358. https://doi.org/10.1007/s10409-017-0666-7
16. Heng S, Guo Y, Yang C, Daemen JJK, Li Z (2015) Experimental and theoretical study of the anisotropic properties of shale. Int J Rock Mech Min Sci 74:58–68. https://doi.org/10.1016/j.ijrmms.2015.01.003
17. Jia L, Chen M, Jin Y, Jiang H (2017) Numerical simulation of failure mechanism of horizontal borehole in transversely isotropic shale gas reservoirs. J Nat Gas Sci Eng 45(88):65–74. https://doi.org/10.1016/j.jngse.2017.05.015
18. Zhang P, Van Dyke M, Su D, Esterhuizen E, Trackemas J (2018) Roof failure in longwall headgates – causes, risks, and prevention, Paper presented at the 52nd U.S. Rock Mechanics/Geomechanics Symposium. Seattle, Washington
19. Shi Q, Mishra B, Wang S, Xu G (2021) In situ assessment of the effectiveness of an undisturbed single driving entry's relief borehole in coal burst-prone seam, *Mining*. Metall Explor 2021:1–10. https://doi.org/10.1007/S42461-021-00511-X
20. Ghabraie B, Ren G, Ghabraie K, Xie YM (2013) A study on truss bolt mechanism in controlling stability of underground excavation and cutter roof failure. Geotech Geol Eng 31(2):667–682. https://doi.org/10.1007/s10706-013-9617-7
21. Shi Q, Mishra B (2020) Discrete element modeling of delamination in laboratory scale laminated rock, *Mining*. Metall Explor 37(5):1–14. https://doi.org/10.1007/s42461-020-00302-w
22. Potyondy DO, Cundall PA (2004) A bonded-particle model for rock. Int J Rock Mech Min Sci 41(8):1329–1364. https://doi.org/10.1016/j.ijrmms.2004.09.011
23. I. Itasca Consulting Group, PFC | US Minneapolis. 2019, Accessed: Jun. 28, 2020. [Online]. Available: https://www.itascacg.com/software/PFC
24. Gadde M, Rusnak J, Honse J, Peng SS (2007) On rock failure criteria for coal measure rocks, in *26th International Conference on Ground Control in Mining, Morgantown, USA*, 2007, pp. 361–369, Accessed: Feb. 28, 2021. [Online]. Available: https://scholar.google.com/scholar?hl=en&as_sdt=0%2C49&q=On+rock+failure+criteria+for+coal+measure+rocks&btnG=
25. Shi Q, Xu G, Wang D, Li Z, Liu W, Wang X (2021) Chain pillar optimization at a longwall coal mine based on field monitoring results and numerical model analysis. Arab J Geosci 2021 1423 14(23):1–8. https://doi.org/10.1007/S12517-021-08843-0
26. Mark C, Molinda GM, Dolinar DR (2001) Analysis of roof bolt systems, 20th Intl Conf on Ground Control in Mining. West Virginia University, Morgantown, WV, pp 218–225
27. Mark C, Molinda GM (1994) Evaluating roof control in underground coal mines with the coal mine roof rating, *Proc. 13th Int. Conf. Gr. Control mining, Morgantown, WV, 1994*, 252–260, https://doi.org/10.1016/0148-9062(95)99821-e
28. Heidari M, Khanlari GR, Kaveh MT, Kargarian S (2012) Predicting the uniaxial compressive and tensile strengths of gypsum rock by point load testing. Rock Mech Rock Eng 45(2):265–273. https://doi.org/10.1007/s00603-011-0196-8
29. Dou F, Wang JG, Zhang X, Wang H (2019) Effect of joint parameters on fracturing behavior of shale in notched three-point-bending test based on discrete element model. Eng Fract Mech 205:40–56. https://doi.org/10.1016/j.engfracmech.2018.11.017
30. Potyondy DO (2017) Simulating perforation damage with a flat-jointed bonded-particle material, Paper presented at the 51st U.S. Rock Mechanics/Geomechanics Symposium. California, USA, San Francisco
31. Gao F, Stead D, Kang H (2014) Simulation of roof shear failure in coal mine roadways using an innovative UDEC Trigon approach. Comput Geotech 61:33–41. https://doi.org/10.1016/J.COMPGEO.2014.04.009
32. Coggan J, Gao F, Stead D, Elmo D (2012) Numerical modelling of the effects of weak immediate roof lithology on coal mine roadway stability. Int J Coal Geol 90–91:100–109. https://doi.org/10.1016/j.coal.2011.11.003
33 Xue Y, Mishra B (2017) Numerical simulation of size effect of laminated rock. Procedia Engineering 191:984–991. https://doi.org/10.1016/j.proeng.2017.05.270
34. Gao F, Stead D (2013) Discrete element modelling of cutter roof failure in coal mine roadways. Int J Coal Geol 116–117:158–171. https://doi.org/10.1016/j.coal.2013.07.020
35. Becker JB (2013) A combined field, laboratory, and numerical study of cutter roof failure in Carroll hollow mine, Master's thesis, University of Akron. http://rave.ohiolink.edu/etdc/view?acc_num=akron1366382367. Accessed 10 Jan 2022
36. Garg P (2018) Behaviour of laminated roof under high horizontal stress, Master's thesis, West Virginia University. https://researchrepository.wvu.edu/etd/7178. Accessed 10 Jan 2022